

# Spin Dynamics of the Centrosymmetric Skyrmion Material GdRu<sub>2</sub>Si<sub>2</sub>

Joseph A. M. Paddison,<sup>1,2,\*</sup> Juba Bouaziz,<sup>3</sup> Andrew F. May,<sup>1</sup> Qiang Zhang,<sup>2</sup> Stuart Calder,<sup>2</sup>  
Douglas Abernathy,<sup>2</sup> Julie B. Staunton,<sup>4</sup> Stefan Blügel,<sup>3</sup> and Andrew D. Christianson<sup>1,†</sup>

<sup>1</sup>Materials Science and Technology Division, Oak Ridge National Laboratory, Oak Ridge, Tennessee 37831, USA

<sup>2</sup>Neutron Scattering Division, Oak Ridge National Laboratory, Oak Ridge, Tennessee 37831, USA

<sup>3</sup>Peter GrÄEnberg Institut and Institute for Advanced Simulation,

Forschungszentrum JÄElich and JARA, 52425 JÄElich, Germany

<sup>4</sup>Department of Physics, University of Warwick, Coventry CV4 7AL, United Kingdom

Magnetic skyrmion crystals are traditionally associated with non-centrosymmetric crystal structures; however, it has been demonstrated that skyrmion crystals can be stabilized by competing interactions in centrosymmetric crystals. To understand and optimize the physical responses associated with topologically-nontrivial skyrmion textures, it is important to quantify their magnetic interactions by comparing theoretical predictions with spectroscopic data. Here, we present neutron diffraction and spectroscopy data on the centrosymmetric skyrmion material GdRu<sub>2</sub>Si<sub>2</sub>, and show that the key spectroscopic features can be explained by the magnetic interactions calculated using density-functional theory calculations. We further show that the recently-proposed 2-**q** “topological spin stripe” structure yields better agreement with our data than a 1-**q** helical structure, and identify how the magnetic structure evolves with temperature.

Magnetic skyrmions are nanometer-scale swirling spin textures that have attracted renewed interest because of their potential applications in high-density magnetic memory technologies [1, 2]. This possibility is based on two properties of skyrmions. First, their nontrivial topology offers them a high degree of protection against external perturbations. Second, magnetic skyrmions can be stabilized by competing (frustrated) magnetic interactions, which can yield skyrmions of smaller dimensions compared with those that are stabilized by the traditional mechanism of antisymmetric exchange interactions [3, 4]. The correspondingly higher skyrmion density can yield larger macroscopic responses, such as topological Hall signals in itinerant-electron materials [5, 6].

The possibility of stabilizing skyrmions by competing interactions has expanded the space of materials candidates to include centrosymmetric systems. Intermetallic materials containing spin-only Gd<sup>3+</sup> or Eu<sup>2+</sup> ions have proved fertile ground for realizing magnetic skyrmion crystals. Skyrmion phases have been discovered where the magnetic ions form different lattice geometries, including triangular in Gd<sub>2</sub>PdSi<sub>3</sub> [5, 7–10], breathing kagome in Gd<sub>3</sub>Ru<sub>4</sub>Al<sub>12</sub> [11], and square in GdRu<sub>2</sub>Si<sub>2</sub> [12–19]. These materials share notably similar magnetic properties. The net magnetic interaction strength, as measured by the Weiss temperature, is ferromagnetic. Long-range magnetic ordering is incommensurate with a periodicity of  $\lesssim 10$  crystallographic unit cells. Applying a magnetic field in the magnetically-ordered phase generates a phase transition to a skyrmion phase—a multi-**q** structure formed by superposing sinusoidal or helical modulations with multiple wavevectors **q**.

The similar magnetic properties of centrosymmetric skyrmion materials suggest that similar interactions are at play; however, the nature of these interactions remains a matter of debate [20–23]. While local magnetic moments reside on the Gd<sup>3+</sup> ions, the magnetic interactions in these intermetallic materials are primarily mediated by conduction electrons [24]. Consequently, magnetic interactions are long-

ranged, presenting challenges for first-principles modeling and experimental parametrization alike. Moreover, the energy resolution of resonant inelastic X-ray measurements is too coarse to resolve the low-energy ( $\sim 5$  meV) magnetic signals in these systems [25]. Therefore, high-quality neutron spectroscopy measurements are crucial to understand the physical responses associated with topologically-nontrivial skyrmion textures.

In this article, we present neutron diffraction and spectroscopy data on the centrosymmetric skyrmion material GdRu<sub>2</sub>Si<sub>2</sub>, and compare its experimental magnetic excitation spectrum with the predictions of state-of-the-art theoretical models [20]. The crystal structure of GdRu<sub>2</sub>Si<sub>2</sub> is tetragonal (space group *I4/mmm*;  $a \approx 4.16$  Å,  $c = 9.60$  Å) and the Gd<sup>3+</sup> ions form a square lattice in the *ab* plane [Figure 1(a)]. We choose GdRu<sub>2</sub>Si<sub>2</sub> to compare with theory because of the apparent simplicity of its crystal structure. This contrasts with Gd<sub>2</sub>PdSi<sub>3</sub>, in which the Pd and Si counter-ions form a superstructure that significantly complicates its magnetic properties [25, 26]. Despite its chemical simplicity, the magnetic behavior of GdRu<sub>2</sub>Si<sub>2</sub> is subtle. It undergoes two magnetic phase transitions upon cooling in zero field, at  $T_N \approx 45$  K and  $T' \approx 38$  K [12, 13, 18]. We will refer to the  $T < T'$  state as Phase 1 and the precursor state at  $T' < T < T_N$  as Phase 4, following Ref. [27]. The zero-field structure below  $T_{N2}$  is a 2-**q** spin texture in which the two wavevectors have slightly different magnitudes, which is referred to as a “topological spin stripe” state because the topological charge of the spin texture exhibits a one-dimensional sinusoidal oscillation [27] and resembles theoretically-proposed structures [28, 29]. In contrast, the magnetic structure of the precursor state is not yet understood; moreover, the interpretation of the Hall signal is challenging in this regime due to thermal spin fluctuations at elevated temperatures [30].

Our study reveals three key results. First, the precursor state at  $T' < T < T_N$  involves a single magnetic propagation vector which splits into two wavevectors with different magnitudes at

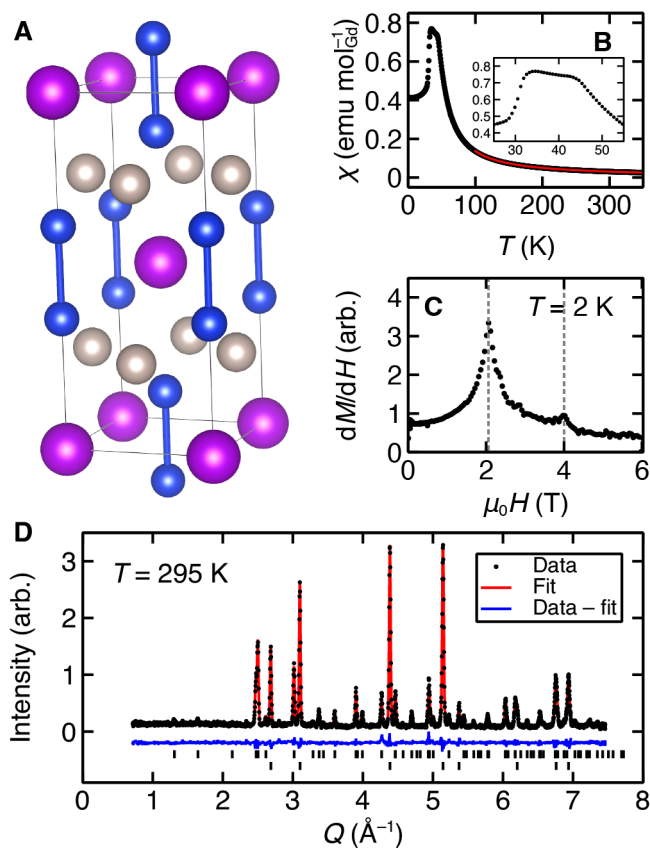


Figure 1. **Structural and magnetic characterization of  $\text{GdRu}_2\text{Si}_2$ .** (a) Crystal structure of  $\text{GdRu}_2\text{Si}_2$ , showing Gd (purple), Ru (grey), and Si (blue) atoms. (b) Magnetic susceptibility measured in a 1 T applied field (black points) and Curie-Weiss fit (red line), indicating  $\mu_{\text{eff}} = 7.978(1) \mu_{\text{B}}$  per Gd and Curie-Weiss temperature 41.63(2) K. (c) Field derivative of magnetization at  $T = 2$  K showing magnetic phase transitions in small applied field. (d) Room-temperature neutron-diffraction data ( $\lambda = 1.536 \text{ \AA}$ ) showing data (black points), Rietveld fit (red line) and data-fit (blue line). The upper tick marks identify nuclear peaks from  $\text{GdRu}_2\text{Si}_2$ , and the lower tick marks identify peaks from the Al sample holder. Refined structural parameters:  $a = 4.165(1) \text{ \AA}$ ,  $c = 9.613(3) \text{ \AA}$ ,  $z(\text{Si}) = 0.367(5)$ ,  $B(\text{Gd}) = 0.47(7) \text{ \AA}^2$ ,  $B(\text{Ru}) = 0.39(6) \text{ \AA}^2$ ,  $B(\text{Si}) = 0.44(8) \text{ \AA}^2$ .

$T'$ , hinting that multi-spin magnetic interactions become more significant on cooling the sample [31]. Second, at low temperature, the key features of our neutron-spectroscopy data are reproduced with high fidelity by the magnetic interactions obtained from density-functional theory [20]. This result reveals that the magnetic Hamiltonian is dominated by isotropic interactions. Third, the agreement with spectroscopic data is improved by assuming the recently-proposed 2- $\mathbf{q}$  topological spin stripe ground state [27], compared to a 1- $\mathbf{q}$  helical ground state [18], providing strong support for the former model. Our results show that first-principles calculations account remarkably well for the magnetic interactions, and place strong constraints on the magnitude and type of interactions that should be included in future models.

We prepared a polycrystalline sample of  $^{160}\text{GdRu}_2\text{Si}_2$  (mass  $\sim 1.3$  g) by arc melting. The use of isotopically-enriched  $^{160}\text{Gd}$  (98.1% enrichment) is essential for successful neutron-scattering experiments, since isotopically natural Gd contains the strongly neutron-absorbing isotopes  $^{155}\text{Gd}$  and  $^{157}\text{Gd}$ . Neutron-scattering experiments were performed at ORNL using a suite of instruments. Room-temperature neutron diffraction data were measured using the HB-2A diffractometer ( $\lambda = 1.536 \text{ \AA}$ ). Low-temperature magnetic diffraction data were measured using the POWGEN diffractometer with a high measured resolution (full width at half maximum) of  $\delta Q/Q = 0.015$  at  $Q = 0.34 \text{ \AA}^{-1}$ . Inelastic measurements were performed using ARCS spectrometer with incident energies  $E_i = 4, 8,$  and  $14$  meV, which covers the bandwidth of magnetic excitations. To reduce the neutron absorption from remaining  $^{155}\text{Gd}$  and  $^{157}\text{Gd}$ , the sample was loaded in an annular geometry into an Al container (HB-2A and ARCS) or V container (POWGEN). Cooling was provided by closed-cycle refrigerators. Our inelastic data were corrected for the energy dependent neutron absorption, which was significant only for  $E_i = 4$  meV, and were placed in absolute intensity units ( $\text{bn sr}^{-1} \text{ meV}^{-1}$  per Gd) by normalization to the nuclear Bragg profile.

The bulk magnetic susceptibility of our sample is shown in Figure 1(b). Our data indicate a magnetic ordering temperature  $T_N \approx 45$  K, and a Curie-Weiss temperature of 41.63(2) K, consistent with previous results [12, 13] and with net ferromagnetic interactions. The bulk susceptibility data show a plateau-like feature between  $\sim 33$  and  $45$  K [inset to Figure 1(b)], which is consistent with the two closely-spaced magnetic phase transitions at  $T_N \approx 45$  K and  $T' \approx 38$  K reported previously [12, 13, 18]. Below, we will discuss the temperature evolution of the zero-field magnetic structure as this feature is crossed. The derivative of the magnetization with respect to applied magnetic field is shown in Figure 1(c), and shows two field-induced magnetic phase transitions at applied fields of approximately 2 and 4 T. Powder neutron-diffraction data collected at room temperature are shown in Figure 1(d), and are quantitatively modeled by the crystal structure shown in Figure 1(a), as demonstrated by the high-quality Rietveld fit.

Having established that the magnetic and crystallographic properties of our sample are consistent with the literature, we turn to the temperature evolution of the zero-field magnetic structure. Figure 2(a) shows the temperature evolution of the neutron diffraction data measured using POWGEN. Below  $T_N$ , a new magnetic peak appears at  $Q \approx 0.34 \text{ \AA}^{-1}$ . As the sample temperature is reduced below  $\approx 35$  K, this peak appears to broaden, and develops into a second peak at smaller  $Q$ . On cooling the sample further, the second peak increases in intensity and in separation from the initial peak. Profile fitting of the diffraction data shown in Figure 2(b-d) reveals that the data collected in Phase 4 ( $T = 42$  K) can be fitted with a single magnetic propagation vector,  $\mathbf{q} = [0.2242(6), 0, 0]$ , whereas data collected in Phase 1 ( $T = 5$  K) require two propagation vectors of different magnitudes,  $\mathbf{q}_1 = [0.2203(2), 0, 0]$

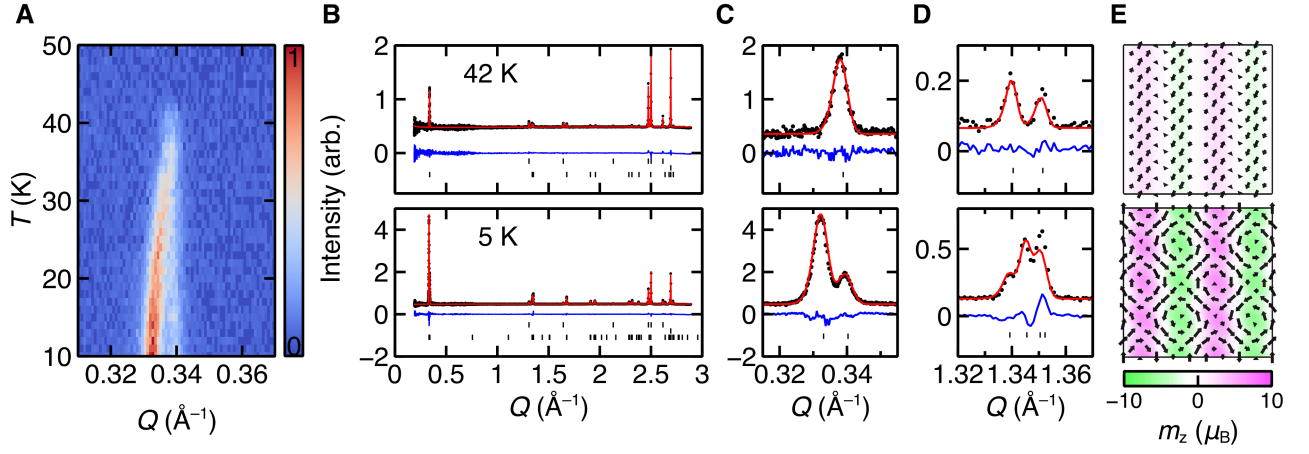


Figure 2. **Neutron diffraction data and Rietveld refinements.** (a) Dependence of the intensity of the magnetic  $(q00)$  reflection, shown in false color, on wavevector magnitude  $Q$  and temperature  $T$ . A single magnetic peak appears at  $T_N \approx 45$  K and splits into two peaks below  $T' \approx 38$  K. (b) Neutron powder diffraction data (black circles), Rietveld fits (red lines), and data-fit (blue lines) at  $T = 42$  K (upper panel) and  $5$  K (lower panel). Tick marks indicate (top to bottom) nuclear, Al, and magnetic peaks. (c) Magnetic  $(q, 0, 0)$  peak at  $42$  K (upper panel) and  $(q_1, 0, 0)$  and  $(q_2, 0, 0)$  peaks at  $5$  K (lower panel). (d) Magnetic  $(1 - q, 0, 1)$  and  $(q, 0, 2)$  peaks at  $42$  K (upper panel), and  $(0, 1 - q_2, 1)$ ,  $(1 - q_1, 0, 1)$ ,  $(q_1, 0, 2)$ , and  $(0, q_2, 2)$  peaks at  $5$  K (lower panel). (e) Graphical representation of the refined  $1\text{-}\mathbf{q}$  sinusoidal magnetic structure at  $42$  K (upper panel) and  $2\text{-}\mathbf{q}$  topological spin-stripe structure including  $\mathbf{q}_1$ , (lower panel). Spin components in the  $ab$  plane are shown as black arrows and the  $c$ -axis spin component is shown in false color.

and  $\mathbf{q}_2 = [0, 0.2251(4), 0]$ . Since  $\mathbf{q} \approx \mathbf{q}_2$ , these results suggest that the phase transition at  $T'$  is associated with the emergence of the additional magnetic propagation vector  $\mathbf{q}_1$ .

To obtain further insight into the temperature evolution of the magnetic structure, we tested structure models against our POWGEN data using magnetic Rietveld refinements. We consider first the data collected in Phase 4 ( $T = 42$  K) and structures of the form [32]

$$\mu(\mathbf{R}) \propto (\mu_a, \mu_b, \mu_c) \exp(-2\pi i \mathbf{q} \cdot \mathbf{R}) + \text{c.c.}, \quad (1)$$

where c.c. denotes the complex conjugate,  $\mathbf{q}$  denotes the propagation vector,  $\mathbf{R}$  denotes a lattice vector, and  $\mu_a, \mu_b, \mu_c$  are (possibly complex) basis-vector components related to unit vectors parallel to the crystallographic  $\mathbf{a}, \mathbf{b}$ , and  $\mathbf{c}$  axes. Initially, we consider an amplitude-modulated sine structure with three real parameters  $\mu_a, \mu_b, \mu_c$ , corresponding to the maximum values of the magnetic moment along  $\mathbf{a}, \mathbf{b}$ , and  $\mathbf{c}$ , respectively. This refinement yields excellent agreement with the  $T = 42$  K experimental data with  $R_{\text{wp}} = 18.0\%$ ; fits to the full profile are shown in Figure 2(b), fits to selected magnetic Bragg peaks in Figures 2(c) and 2(d), and a graphical representation of the refined structure is shown in Figure 2(e). Refined values of the basis-vector components for all models are given in Table I. The refined values of  $\mu_b$  and  $\mu_c$  are equal within error, while  $\mu_a$  is much smaller, suggesting that a sine structure with magnetic moments polarized along the  $[011]$  direction is an appropriate single-parameter model. This model yields a very similar fit quality ( $R_{\text{wp}} = 18.1\%$ ) to the three parameter model. Due to the effect of powder averaging, however, the sine structure with  $[011]$  moment direction is not a unique solution: a helical magnetic structure with magnetic moments confined to the  $bc$  plane yields an identical fit.

These models are physically distinct: in particular, in the helical case, the magnetic moment length is the same on every site in the crystal, whereas in the sine case, the magnetic moment amplitude is modulated. The magnetic moment does not exceed the maximum expected value of  $7.0 \mu_B$  per Gd for either model, so both models are physically reasonable; moreover, several examples are known where an amplitude-modulated magnetic structure exists at elevated temperatures (e.g., [33–35]). Further experiments, such as single-crystal neutron diffraction, would be needed to distinguish between the sine and helical possibilities.

At our base temperature of  $5$  K, we compare our powder neutron diffraction data with the topological spin-stripe structure [27] shown in Figure 2(e). The moment orientations in this model are a sum of three components [27],

$$\begin{aligned} \mu_{\text{LT}}(\mathbf{R}) \propto & (0, \mu_1, i\mu_1) \exp(-2\pi i \mathbf{q}_1 \cdot \mathbf{R}) \\ & + (\mu_2, 0, 0) \exp(-2\pi i \mathbf{q}_2 \cdot \mathbf{R}) \\ & + (0, \mu_3, i\mu_3) \exp(-2\pi i \mathbf{q}_3 \cdot \mathbf{R}) + \text{c.c.}, \end{aligned}$$

which are a circular helix with moments in the  $bc$  plane with propagation vector  $\mathbf{q}_1$ , an amplitude-modulated sine structure with moments along  $[100]$  with propagation vector  $\mathbf{q}_2$ , and a second circular helix with propagation vector  $\mathbf{q}_3 = \mathbf{q}_1 + 2\mathbf{q}_2$ . The inclusion of  $\mathbf{q}_3$  with  $\mu_3 = \mu_2^2/4\mu_1$  constrains the magnitude of the magnetic moment to be the same on all sites in the crystal [27]. Our powder data provide a particularly stringent test of this model, since their high resolution allow peaks associated with  $\mathbf{q}_1$  and  $\mathbf{q}_2$  to be clearly resolved. First, we allow  $\mu_1, \mu_2$ , and  $\mu_3$  to refine independently, which yields excellent agreement with the experimental data ( $R_{\text{wp}} = 17.6\%$ ). The refined values of  $\mu_1, \mu_2$ , and

$T$ (K)	Structure type	$\mathbf{q}$ (r.l.u.)		$\mu_{\parallel\mathbf{a}}$ ( $\mu_B$ )	$\mu_{\parallel\mathbf{b}}$ ( $\mu_B$ )	$\mu_{\parallel\mathbf{c}}$ ( $\mu_B$ )	$\max(\mu_{\text{ord}})$ ( $\mu_B$ )	$R_{\text{wp}}$ (%)
42	Sine	[0.2242(6), 0, 0]		1.00(23)	2.17(13)	2.39(12)	3.38(14)	18.0
42	Sine			0*	2.32(3) <sup>†</sup>	2.32(3) <sup>†</sup>	3.28(5)	18.1
42	Helical			0*	2.32(3) <sup>†</sup>	2.32(3) <sup>†</sup> $i$	2.32(3)	18.1
		$\mathbf{q}_1$ (r.l.u.)	$\mathbf{q}_2$ (r.l.u.)	$\mu_1$ ( $\mu_B$ )	$\mu_2$ ( $\mu_B$ )	$\mu_3$ ( $\mu_B$ )		
5	Multi- $\mathbf{q}$	[0.2203(2), 0, 0]	[0, 0.2251(4), 0]	5.45(3)	4.63(5)	0.65(17)	7.18(5)	17.6

Table I. Fitted values of magnetic structure parameters from Rietveld refinements. The derived maximum value of the ordered magnetic moment per Gd is also given. Values denoted with a dagger (<sup>†</sup>) were constrained to be of equal magnitude. Parameter uncertainties indicate  $1\sigma$  confidence intervals.

$\mu_3$  and  $\mathbf{q}_1$  and  $\mathbf{q}_2$  are in good agreement with Ref. [27] (see Table I). Peaks associated with  $\mathbf{q}_3$  are not directly resolved, but the value of  $\mu_3$  is constrained by the overall goodness-of-fit. Notably, in our refinements,  $\mathbf{q}_1$  and  $\mathbf{q}_2$  are swapped compared to Ref. [27], so that the smaller wavevector corresponds to the helical modulation and the larger wavevector to the sinusoidal one; this choice is necessary to obtain satisfactory agreement with our data. Second, we constrain the ratios  $\mu_2/\mu_1$  and  $\mu_3/\mu_1$  to be the same as Ref. [27], and refine only the magnitude of  $\mu_1$ . This procedure ensures that the magnetic moment is identical on all sites in the crystal, and again yields good agreement with the data ( $R_{\text{wp}} = 17.6\%$ ). The refined magnetic moment magnitude of  $6.98(2)\mu_B$  per Gd is in excellent agreement with the spin-only value of  $7.0\mu_B$  for spin-only  $\text{Gd}^{3+}$  ions. Therefore, our refinements of high-resolution powder neutron diffraction data provide strong support for the 2- $\mathbf{q}$  topological-spin-stripe ground state.

With a model of the magnetic ground-state structure in hand, we now investigate the low-energy spin dynamics. Traditionally, such analysis proceeds by optimizing a few magnetic exchange parameters against inelastic neutron scattering data. However, this approach provides at best an effective description of intermetallic magnets such as  $\text{GdRu}_2\text{Si}_2$ , because the long-ranged nature of the RKKY interactions implies that an impractically large number of interaction parameters must be optimized for a complete description. For this reason, we instead compare our inelastic neutron-scattering data with predictions of the density-functional-theory (DFT) simulations reported in Ref. [20], which provide a qualitatively correct description of the magnetic field *vs.* temperature phase diagram of  $\text{GdRu}_2\text{Si}_2$  [20]. The DFT interactions describe an isotropic (Heisenberg) Hamiltonian,

$$H_{\text{iso}} = - \sum_{i>j} J_{ij} \mathbf{S}_i \cdot \mathbf{S}_j,$$

where  $\mathbf{S}_i$  denotes a spin vector with position  $\mathbf{R}_i$  and quantum number  $S = 7/2$ , and  $J_{ij} \equiv J(\mathbf{R}_j - \mathbf{R}_i)$  is the interaction between spins at  $\mathbf{R}_i$  and  $\mathbf{R}_j$ . The dependence of the DFT interactions on radial distance,  $r = |\mathbf{R}_j - \mathbf{R}_i|$ , is shown in Figure 3(a). While the magnitudes of the interactions decay rapidly with increasing distance, treating their long-ranged nature is nevertheless crucial: A maximum distance of  $10a = 41.6\text{ \AA}$  is needed to obtain a calculated magnetic propagation vector  $\mathbf{q}_{\text{calc}} = [0.184, 0, 0]$  in reasonable agreement with the experimental value, whereas truncating the interactions at a dis-

tance of  $3a$  yields an incorrect ferromagnetic propagation vector  $\mathbf{q}_{\text{calc}} = \mathbf{0}$ . The long-range nature of the interactions hints towards an RKKY mechanism [20].

Figure 3(b–e) compares our inelastic neutron-scattering data with calculations of the magnetic excitation spectra performed using linear spin-wave theory. Figure 3(b) shows constant- $Q$  cuts of the experimental data, while the top panels of Figure 3(c), (d), and (e) show data collected with  $E_i = 4, 8,$  and  $14$  meV, respectively. Our data show an overall excitation bandwidth of approximately 4.5 meV. The  $E_i = 4$  meV data clearly show a region of high intensity at  $0.5 \lesssim E \lesssim 1.0$  meV at small  $Q$ , while the  $E_i = 8$  meV data suggest that the spectral weight at  $E \sim 3$  meV consists of two nearly-dispersionless excitation bands at  $E \approx 2.8$  and  $3.2$  meV. To model our inelastic neutron-scattering data, we calculate the neutron-scattering spectrum using linear spin-wave theory, as implemented in the SpinW program [36]. The Hamiltonian is the sum of the isotropic interactions calculated by DFT (see Figure 3(a)) and the long-ranged dipolar interaction, so that the total Hamiltonian is given by

$$H = H_{\text{iso}} + D \sum_{i>j} \frac{\mathbf{S}_i \cdot \mathbf{S}_j - 3(\mathbf{S}_i \cdot \hat{\mathbf{r}}_{ij})(\mathbf{S}_j \cdot \hat{\mathbf{r}}_{ij})}{(r_{ij}/r_1)^3},$$

where  $D = 0.047$  meV is the energy scale of the dipolar interaction at the nearest-neighbor distance  $r_1$ , which is proportional to the squared magnetic moment and is thus relatively large for  $\text{Gd}^{3+}$ . We also include a small easy-axis single-ion anisotropy term,  $\Delta = -0.005$  meV, to stabilize magnetic moments in the  $bc$  plane.

Importantly, linear spin-wave theory requires a magnetically ordered state that is a local energy minimum of the assumed magnetic Hamiltonian. If there is more than one such state, each may have a distinct magnetic excitation spectrum [37]. In  $\text{GdRu}_2\text{Si}_2$ , the magnetic Gd ions occupy a Bravais lattice, and the DFT calculation includes Heisenberg magnetic interactions only. In this case, the magnetic ground state of the Hamiltonian is a 1- $\mathbf{q}$  helix. This result is not fully consistent with the experimental result from neutron diffraction, which shows that the observed magnetic ground state is actually a 2- $\mathbf{q}$  state. However, since the largest basis-vector component in the 2- $\mathbf{q}$  structure describes a helix, and the neutron-scattering intensity is proportional to the square of the basis-vector component magnitude, we expect that scattering from the helical component will make the largest contribution to the observed intensity. The calculated spin-wave spectrum of the helical

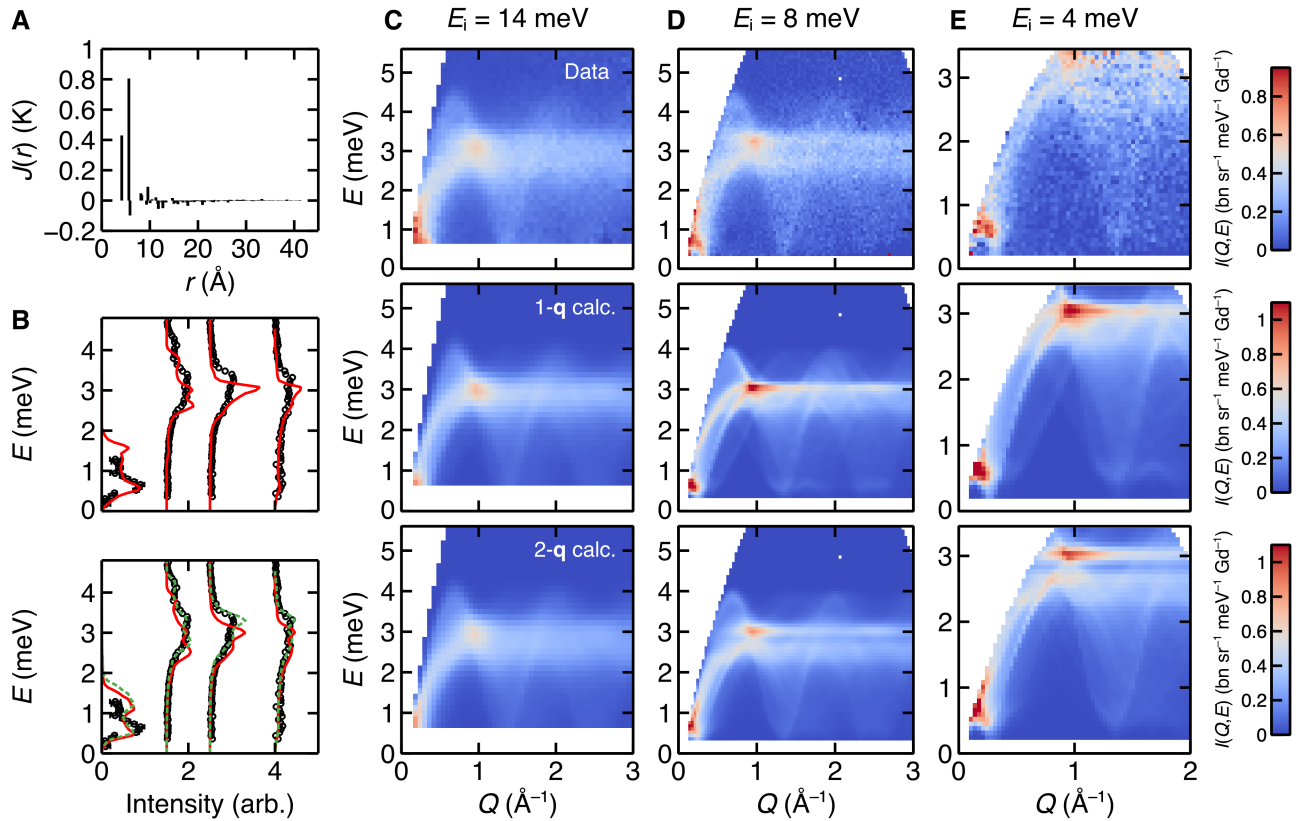


Figure 3. **Inelastic neutron scattering data and spin-wave model calculations.** (a) Dependence of magnetic interactions  $J(r)$  determined from DFT calculations [20] on radial distance  $r$ . Positive values indicate ferromagnetic interactions. (b) Constant- $Q$  cuts of inelastic neutron-scattering data compared with linear-spin-wave calculations, showing cuts at (left to right)  $Q = 0.245, 0.735, 0.980,$  and  $1.330 \text{\AA}^{-1}$ . Cuts are from  $E_i = 4$  meV ( $Q = 0.245 \text{\AA}^{-1}$ ) and 8 meV data (all other cuts) and the  $Q$ -resolution is  $\pm 0.0175 \text{\AA}^{-1}$ . Calculations are for  $J(r)$  and the  $1\text{-q}$  helical structure (red lines in upper panel),  $J(r)$  and the  $2\text{-q}$  topological spin stripe structure (red lines in lower panel), and  $1.1J(r)$  in the  $2\text{-q}$  topological spin stripe structure (dotted green lines in lower panel). (c) Data with  $E_i = 14$  meV (top panel),  $1\text{-q}$  spin-wave calculation (middle panel), and  $2\text{-q}$  calculation (lower panel). (d) Data with  $E_i = 8$  meV (top panel),  $1\text{-q}$  spin-wave calculation (middle panel), and  $2\text{-q}$  calculation (lower panel). (e) Data with  $E_i = 4$  meV (top panel),  $1\text{-q}$  spin-wave calculation (middle panel), and  $2\text{-q}$  calculation (lower panel). All calculations are convolved with the instrumental energy resolution of 0.52, 0.23, and 0.13 meV for  $E_i = 14, 8,$  and  $4$  meV, respectively, from Gaussian fits to the elastic line of the experimental data.

state is shown in the upper panel of Figure 3(b) and the middle panels of Figure 3(c), (d), and (e). The overall energy scale agrees well with the experimental data and the main features of the data are well reproduced. This level of agreement is remarkable, considering that the comparison relies on independent first-principles calculations [20] and does not include any free parameters.

We now consider the excitation spectrum of the  $2\text{-q}$  topological-spin-stripe state [27]. Compared to the  $1\text{-q}$  helical state, this calculation introduces two complexities. First, to account for the multi- $\mathbf{q}$  state, it is necessary to use a supercell of the crystallographic unit cell; we consider a  $5 \times 5 \times 1$  supercell containing 50  $\text{Gd}^{3+}$  ions, which enforces propagation vectors of  $[\frac{1}{5}, 0, 0]$  and  $[0, \frac{1}{5}, 0]$ . Second, the  $2\text{-q}$  ground state has an energy  $\approx 2.8\%$  greater than that of the helical state; hence, it is not an exact local energy minimum of the Hamiltonian. These two limitations imply that the spin-wave energies contain some imaginary values, which are unphysi-

cal and must be discarded in the calculation of the spin-wave intensities [38]. Since only a small fraction ( $\approx 0.06\%$ ) of the spin-wave modes considered have imaginary eigenvalues, we expect that the calculated spectrum still represents a reasonable approximation to the spin-wave spectrum of the  $2\text{-q}$  ground state. The excitation spectrum of the  $2\text{-q}$  topological-spin-stripe state is shown in the upper panel of Figure 3(b), and the lower panels of Figure 3(c), (d), and (e). It shows clearly improved agreement with the experimental data compared to the  $1\text{-q}$  helical calculation. Notably, the  $2\text{-q}$  calculation reproduces the two nearly-dispersionless excitation bands at  $E \approx 2.8$  and  $3.2$  meV that are not reproduced by the helical calculation. The agreement with experiment is further improved by scaling the energies of all the interactions by a factor of 1.1. This scaling provides essentially quantitative agreement between the  $2\text{-q}$  calculation and the experimental data, as shown by the constant- $Q$  cuts in the lower panel of Figure 3(b). It also yields improved agreement between

the experimental Weiss temperature (41 K) and the calculated value obtained as  $\theta_{\text{calc}} = \frac{1}{3}S(S+1)\sum_j Z_j J_{0j}$ , which is 28 K after rescaling.

Our neutron-scattering experiments provide an essential quantitative test of the magnetic interactions of GdRu<sub>2</sub>Si<sub>2</sub> calculated from first-principles theory. Our results show that the theoretical calculations [20] provide an accurate description of our experimental data, providing confirmation of the methodology and the nature of the interactions. In particular, our study indicates that the magnetic interactions of GdRu<sub>2</sub>Si<sub>2</sub> are dominated by isotropic (Heisenberg) exchange, and the long-ranged nature of the DFT interactions strongly supports interpretations in terms of a generalized RKKY mechanism [20, 23, 25]. This mechanism is supported by quantum-oscillation measurements in GdRu<sub>2</sub>Si<sub>2</sub> [24], but is not universal in magnetic intermetallics, where superexchange can dominate [39]. The excellent agreement of first-principles calculations with experimental data also shines light on the few areas in which the theory does *not* fully agree with experiment. Most importantly, our experimental results confirm the 2-**q** nature of the magnetic ground state, but this state cannot be stabilized by purely isotropic interactions; an anisotropic or multi-spin contribution is necessary to stabilize it; two possible candidates are a biquadratic interaction [28] or a bond-dependent anisotropy [29]. However, the excellent agreement of the purely isotropic model with our spectroscopic model suggests that the anisotropic contribution is much smaller than the isotropic one. As such, the determination of this contribution represents an open challenge for theory and experiment alike, which motivates further experiments on single-crystal samples [29].

We are grateful to Geetha Balakrishnan (Warwick), Eleanor Clements (ORNL), Shang Gao (ORNL), and George Wood (Warwick) for valuable discussions. This work was supported by the U.S. Department of Energy, Office of Science, Basic Energy Sciences, Materials Sciences and Engineering Division, and used resources at the High Flux Isotope Reactor and Spallation Neutron Source, DOE Office of Science User Facilities operated by the Oak Ridge National Laboratory. The isotope used in this research was supplied by the U.S. Department of Energy Isotope Program, managed by the Office of Isotope R&D and Production.

---

\* paddisonja@ornl.gov

† christiansad@ornl.gov

- [1] A. N. Bogdanov, C. Panagopoulos, *Nat. Rev. Phys.* **2**, 492 (2020).
- [2] Y. Tokura, N. Kanazawa, *Chem. Rev.* **121**, 2857 (2021).
- [3] T. Okubo, S. Chung, H. Kawamura, *Phys. Rev. Lett.* **108**, 017206 (2012).
- [4] A. O. Leonov, M. Mostovoy, *Nat. Commun.* **6**, 8275 (2015).
- [5] T. Kurumaji, *et al.*, *Science* **365**, 914 (2019).
- [6] X. Yao, J. Chen, S. Dong, *New J. Phys.* **22**, 083032 (2020).
- [7] R. Mallik, E. V. Sampathkumaran, M. Strecker, G. Wortmann, *Europhys. Lett. (EPL)* **41**, 315 (1998).
- [8] H. Zhang, *et al.*, *New J. Phys.* **22**, 083056 (2020).
- [9] E. V. Sampathkumaran, I. Das, R. Rawat, S. Majumdar, *App. Phys. Lett.* **77**, 418 (2000).
- [10] M. Hirschberger, *et al.*, *Phys. Rev. B* **101**, 220401 (2020).
- [11] M. Hirschberger, *et al.*, *Nat. Commun.* **10**, 5831 (2019).
- [12] A. Garnier, *et al.*, *J. Magn. Magn. Mater.* **140-144**, 899 (1995). International Conference on Magnetism.
- [13] A. Garnier, D. Gignoux, D. Schmitt, T. Shigeoka, *Physica B: Condensed Matter* **222**, 80 (1996).
- [14] N. D. Khanh, *et al.*, *Nat. Nanotechnol.* **15**, 444 (2020).
- [15] N. D. Khanh, *et al.*, *Advanced Science* **9**, 2105452 (2022).
- [16] M. Rotter, *et al.*, *J. Magn. Magn. Mater.* **310**, 1383 (2007). Proceedings of the 17th International Conference on Magnetism.
- [17] T. Samanta, I. Das, S. Banerjee, *J. Appl. Phys.* **104**, 123901 (2008).
- [18] Y. Yasui, *et al.*, *Nat. Commun.* **11**, 5925 (2020).
- [19] S. V. Eremeev, *et al.*, *Nanoscale Adv.* **5**, 6678 (2023).
- [20] J. Bouaziz, E. Mendive-Tapia, S. Blügel, J. B. Staunton, *Phys. Rev. Lett.* **128**, 157206 (2022).
- [21] T. Nomoto, T. Koretsune, R. Arita, *Phys. Rev. Lett.* **125**, 117204 (2020).
- [22] S. Hayami, Y. Motome, *Phys. Rev. B* **103**, 024439 (2021).
- [23] T. Nomoto, R. Arita, *J. Appl. Phys.* **133**, 150901 (2023).
- [24] N. Matsuyama, *et al.*, *Phys. Rev. B* **107**, 104421 (2023).
- [25] J. A. M. Paddison, *et al.*, *Phys. Rev. Lett.* **129**, 137202 (2022).
- [26] F. Tang, *et al.*, *Phys. Rev. B* **84**, 104105 (2011).
- [27] G. D. A. Wood, *et al.*, *Phys. Rev. B* **107**, L180402 (2023).
- [28] R. Ozawa, *et al.*, *J. Phys. Soc. Jpn.* **85**, 103703 (2016).
- [29] S. Hayami, Y. Motome, *Phys. Rev. B* **103**, 054422 (2021).
- [30] H. Ishizuka, N. Nagaosa, *Science Advances* **4**, eaap9962 (2018).
- [31] E. Mendive-Tapia, J. B. Staunton, *Phys. Rev. Lett.* **118**, 197202 (2017).
- [32] A. Wills, *J. Phys. IV France* **11**, 133 (2001).
- [33] Z. Islam, *et al.*, *Phys. Rev. B* **58**, 8522 (1998).
- [34] J. A. Blanco, *et al.*, *Phys. Rev. B* **82**, 054414 (2010).
- [35] E. Mendive-Tapia, J. B. Staunton, *Phys. Rev. B* **99**, 144424 (2019).
- [36] S. Toth, B. Lake, *J. Phys.: Condens. Matter* **27**, 166002 (2015).
- [37] J. A. M. Paddison, *et al.*, *npj Quantum Mater.* **6**, 99 (2021).
- [38] X. Bai, *et al.*, *Phys. Rev. Lett.* **122**, 097201 (2019).
- [39] J. Bouaziz, G. Bihlmayer, C. E. Patrick, J. B. Staunton, S. Blügel, *Phys. Rev. B* **109**, L201108 (2024).